# On Drell-Yan production of scalar leptoquarks coupling to heavy-quark flavours

**Ulrich Haisch,**[a] **Luc Schnell**[a,b] **and Stefan Schulte**[a,b]

[a]*Max Planck Institute for Physics,*
*Föhringer Ring 6, München 80805, Germany*

[b]*Technische Universität München, Physik-Department,*
*James-Franck-Strasse 1, Garching 85748, Germany*

*E-mail:* haisch@mpp.mpg.de, schnell@mpp.mpg.de, sschulte@mpp.mpg.de

ABSTRACT: Given the hints of lepton-flavour non-universality in semi-leptonic $B$ decays, leptoquark (LQ) models with sizeable couplings to heavy-quark flavours are enjoying a renaissance. While such models are subject to stringent constraints from low-energy experiments also bounds from non-resonant dilepton searches at the Large Hadron Collider (LHC) turn out to be phenomenologically relevant. Based on the latest LHC dilepton analyses corresponding to an integrated luminosity of around $140 \, \text{fb}^{-1}$ of proton-proton collisions at $\sqrt{s} = 13 \, \text{TeV}$, we present improved limits on the scalar LQ couplings that involve heavy-quark flavours and light or heavy dileptons. In particular, we show that effects beyond the leading order that are related to real QCD emissions are relevant in this context, since the inclusion of additional heavy-flavoured jets notably improves the exclusion limits that derive from the high-mass dilepton tails. The impact of electroweak corrections and interference effects between signal and background is also analysed. Within the `POWHEG-BOX` framework we provide a dedicated Monte Carlo code that allows for an on-the-fly signal event generation including all the LQ corrections considered in this article.

# Contents

# 1 Introduction

Measurements of Drell-Yan (DY) production represent a pillar of the research programme at the Large Hadron Collider (LHC). These searches are possible owing to the clean and well reconstructable experimental signature with excellent detection efficiency. While in the context of physics beyond the Standard Model (SM) both ATLAS and CMS have mostly investigated resonant dilepton signatures, recently also searches for non-resonant phenomena leading to dilepton final states [1–6] have been performed.

Investigating non-resonant phenomena in DY production involving both light ($e^+e^-$ or $\mu^+\mu^-$) and heavy ($\tau^+\tau^-$) dilepton pairs is theoretically well motivated [7–27] given the persisting hints of lepton-flavour universality violation that have been observed in the $b \to c\ell\nu$ [28–33] and $b \to s\ell^+\ell^-$ [34–38] systems. An apparent link between these flavour anomalies and non-resonant modifications in DY dilepton distributions arises in leptoquark (LQ) models with sizeable couplings to heavy-quark flavours, where $t$-channel LQ exchange contributes to $pp \to \ell^+\ell^-$ production at the tree level. In LQ models of this type the enhancement of new-physics effects at high energies can be utilised to curb the limited precision of the existing DY dilepton measurements, allowing the bounds obtained in this way to be both complementary and competitive with those derived from precision low-energy data. It has also been noticed [1, 4, 6, 12, 18, 39–43] that the sensitivities to models that provide an explanation of the anomalies in semileptonic $B$ decays may be improved by requiring an additional jet containing the decay of a $B$ hadron ($b$-jet) in the final state.

The main goal of this article is to refine the theoretical description of DY production in scalar LQ models (see also [44–53] for publications similar in spirit). To this purpose we calculate the next-to-leading order (NLO) QCD corrections to $pp \to \ell^+\ell^-$ production. This computation involves the evaluation of the real and virtual corrections to the $t$-channel Born-level contribution as well as the calculation of resonant single-LQ production followed by the decay of the LQ. Such a calculation has been performed in the case of first- and second-generation LQs already in the article [54] but not for third-generation LQs, which is the main focus here. Besides QCD corrections we also consider the phenomenological impact of electroweak (EW) corrections and study the size of interference effects between the leading order (LO) LQ signal and the LO SM background. These fixed-order predictions are consistently matched to a parton shower (PS) employing the `POWHEG` method [55, 56] as automatised in the `POWHEG-BOX` [57]. This allows for a realistic exclusive description of DY dilepton processes in scalar LQ models at the level of hadronic events. In particular, our `POWHEG` implementation can generate events with one additional parton from the matrix element calculation without the need to introduce a merging or matching scale. This enables us to study the constraints on scalar LQ models that derive from the DY searches in high-mass dimuon ($\mu^+\mu^-$) final states without [2] and with a $b$-jet [4]. Finally, we also determine the restrictions that the latest ditau ($\tau^+\tau^-$) search [6] put on scalar LQ models studying two different $b$-jet categories. Based on our DY analyses we are able to derive improved limits on the parameter space of third-generation scalar LQ models using the full LHC Run II integrated luminosity of around $140\,\mathrm{fb}^{-1}$ obtained for proton-proton ($pp$) collisions at a centre-of-mass energy of $\sqrt{s} = 13\,\mathrm{TeV}$.

The remainder of this article is organised in the following way. In section 2 we specify the structure of the LQ interactions that we consider in this work. Section 3 briefly describes the basic ingredients of the calculations of the different LQ contributions to DY production and their implementation into the `POWHEG-BOX`. The impact of the different types of LQ corrections on the kinematic distributions in $pp \to \ell^+\ell^-$ production is presented in section 4. Our recasts of the LHC searches [2, 4, 6] are discussed in section 5, where we also derive improved limits on the Yukawa couplings and masses of third-generation scalar LQs. We conclude and present an outlook in section 6. Constraints on the parameter space of second-generation scalar LQs are provided in the supplementary material that can be found in appendix A.

## 2 Theoretical framework

LQs are hypothetical coloured bosons that carry both baryon and lepton number [58]. They therefore often emerge in beyond the SM (BSM) models that unify matter [59]. Since any viable theory of unification has to reduce at low energies to the SM such that the particle phenomenology observed in experiments is reproduced, scalar LQs can only appear in five different representations [60, 61]. In order to illustrate the possible effects of scalar LQ contributions to DY dilepton processes, we focus on the following simplified LQ model

$$\mathcal{L} \supset Y_{u\ell}\, \bar{u}^c \ell\, S_1^\dagger + Y_{d\ell}\, \bar{d}^c \ell\, \tilde{S}_1^\dagger + \mathrm{h.c.}\,, \tag{2.1}$$
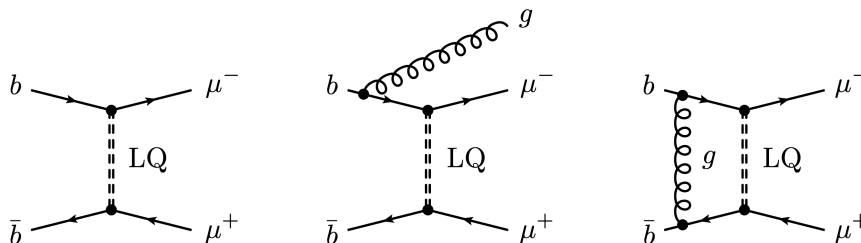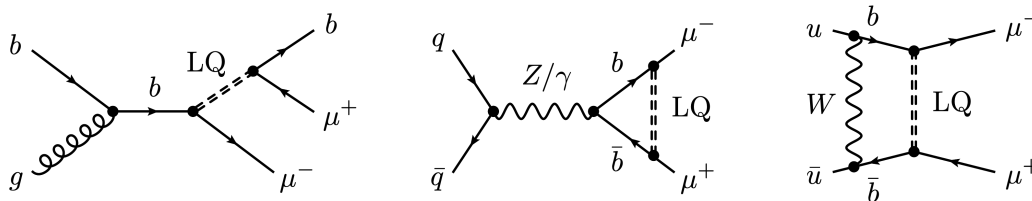
**Figure 1**. Examples of LQ contributions to DY dimuon production initiated by bottom-quark fusion. The left Feynman diagram describes the tree-level process involving $t$-channel LQ exchange, while the middle (right) graph represents the corresponding real (virtual) QCD corrections. See main text for further details.

where $u, d$ and $\ell$ represent the right-handed up-type, down-type quarks and charged lepton fields, respectively, and the superscript $c$ denotes charge conjugation. The fermionic SM fields are understood to be mass eigenstates, i.e. the states that lead to diagonal SM Yukawa coupling matrices after spontaneous EW symmetry breaking. The couplings $Y_{u\ell}$ and $Y_{d\ell}$ are complex $3 \times 3$ matrices in flavour space, while the fields $S_1$ and $\tilde{S}_1$ correspond to the two $\mathrm{SU}(2)_L$ LQ singlets allowed by gauge invariance. Explicitly, the LQ fields transform as $S_1 \sim (3, 1, -1/3)$ and $\tilde{S}_1 \sim (3, 1, -4/3)$ under the full $\mathrm{SU}(3)_C \times \mathrm{SU}(2)_L \times \mathrm{U}(1)_Y$ SM gauge group. Notice that the size of the modifications in $pp \to \ell^+\ell^-$ production due to LQ exchange depends primarily on the flavour structure and the magnitude of the couplings $Y_{u\ell}$ and $Y_{d\ell}$. However, once interference effects between the LQ signal and the SM background are considered also the representation of the LQ plays a role because the interference pattern depends on the quantum numbers of the exchanged LQ [21]. In fact, in the case of $S_1$ ($\tilde{S}_1$) it turns out that the above Lagrangian gives rise to destructive (constructive) interference of the LQ signal with the SM DY background. The interactions (2.1) can therefore be used as a template to cover the full space of scalar LQ models which entails besides the $\mathrm{SU}(2)_L$ singlets $S_1$ and $\tilde{S}_1$ the $\mathrm{SU}(2)_L$ doublets $S_2$ and $\tilde{S}_2$ and an $\mathrm{SU}(2)_L$ triplet $S_3$. In this context, we add that the fields $S_2$ and $S_3$ lead to constructive interference, while $\tilde{S}_2$ interferes destructively with the SM DY background.

## 3   Calculation in a nutshell

Figures 1 and 2 display representative Feynman diagrams inducing DY dimuon production in the presence of (2.1). The first figure shows the tree-level contribution involving $t$-channel LQ exchange (left) and the corresponding real (middle) and virtual (right) QCD corrections. Notice that all depicted contributions are initiated by bottom-quark ($b\bar{b}$) fusion[1] and that the exchanged LQ is an $\tilde{S}_1$. An assortment of LQ contributions to DY dimuon production that arise beyond the LO in perturbation theory is given in the second figure. The left Feynman diagram gives rise to resonant single-LQ production with subsequent decay of the LQ to a pair of a bottom quark and an anti-muon, i.e. $gb \to \tilde{S}_1 \mu^-$ with $\tilde{S}_1 \to b\mu^+$.

---

[1]Throughout this article we work in the five-flavour scheme, where charm- and bottom-quarks are considered as partons in the proton and as such have a corresponding parton distribution function (PDF).

**Figure 2**. An assortment of LQ contributions to DY dimuon production that arise beyond the leading order in perturbation theory. The left graph is an example of resonant single-LQ production followed by the decay of the LQ, whereas the middle and right diagram represent EW corrections involving LQ exchange. For additional explanations consult the main text.

Notice that graphs of this type as well as the real and virtual corrections shown in figure 1 all represent a $\mathcal{O}(\alpha_s)$ correction to the inclusive DY dilepton production rate. In order to achieve NLO accuracy in QCD one therefore has to include all three classes of graphs. Notice that the diagrams in figure 1 and the left graph in figure 2 with bottom replaced by charm quarks arise in the case of the LQ singlet $S_1$.

Besides QCD corrections to $pp \to \ell^+\ell^-$ we also consider EW effects to DY production in our article. Two prototype graphs of this kind are shown in the centre and on the right-hand side of figure 2. The first type of diagrams encodes the virtual corrections to the $Z\ell^+\ell^-$ and $\gamma\ell^+\ell^-$ vertices involving the exchange of an LQ. These vertex corrections appear both in the initial and the final state. The second type of EW corrections is associated to one-loop Feynman graphs with $W$-boson exchange. Notice that due to the structure of (2.1), which only involves right-handed fermionic fields, EW contributions of the latter kind are strongly chirally suppressed by small SM Yukawa couplings. In the case of DY production by heavy-quark fusion these corrections furthermore involve small Cabibbo-Kobayashi-Maskawa matrix elements. We therefore do not include EW corrections related to $W$-boson exchange in our analysis. Likewise, we also do not consider EW contributions due to SM Higgs-boson exchange, because these corrections are again insignificant as they are proportional to small SM Yukawa couplings.

The third kind of quantum effects that we consider in our work is the interference between the LQ and the SM contributions to tree-level $q\bar{q} \to \ell^+\ell^-$ scattering. We treat these contributions at the LO in perturbation theory, which means that our `POWHEG-BOX` implementation contains the squared matrix elements built from the $t$-channel LQ contribution and the SM corrections involving $Z$-boson or photon exchange in the $s$-channel.

All matrix elements are computed using conventional dimensional regularisation for both ultraviolet (UV) and infrared (IR) singularities. The actual generation and computation of squared matrix elements relies on the `Mathematica` packages `FeynRules` [62], `FeynArts` [63], `FormCalc` [64], `LoopTools` [65] and `Package-X` [66]. Our calculation of NLO QCD and EW effects is performed in the on-shell scheme. In order to deal with the soft and collinear singularities of the real corrections to the $t$-channel LQ exchange contribution, cf. the middle diagram in figure 1, and to cancel the IR poles of the one-loop virtual corrections, cf. the right diagram in figure 1, we exploit the general implementation of the Frixione-Kunszt-Signer subtraction [67, 68] within the `POWHEG-BOX` framework. For

this purpose, the full `POWHEG-BOX` machinery is used that automatically builds the soft and collinear counterterms and remnants, and also checks the behaviour in the soft and collinear limits of the real squared matrix elements against their soft and collinear approximations. Notice that the real NLO QCD contributions that describe resonant single-LQ production with subsequent decay of the LQ are IR finite and therefore do not require a subtraction (cf. the left diagram in figure 2). Our Monte Carlo (MC) code therefore allows to achieve NLO+PS accuracy for DY dilepton production in any scalar LQ model described by (2.1). In particular, our `POWHEG` implementation is able to generate events with one additional parton from the matrix element calculation without the need to introduce a merging or matching scale. Two-jet events are instead exclusively generated by the PS in our MC setup.

Let us finally add that the results of our calculation of the virtual corrections to the $Z\ell^+\ell^-$ and $\gamma\ell^+\ell^-$ vertices involving the exchange of a LQ can be shown to resemble the leading terms in the heavy-mass expansion of the corresponding form factors given in the publication [69]. This comparison serves as a useful cross-check of our computation.

## 4 Phenomenological analyses

In this section we discuss the numerical impact of the different types of LQ corrections on the kinematic distributions that are most relevant for the existing LHC searches for non-resonant BSM physics in dilepton final states. The case of light and heavy dilepton pairs is discussed separately and in both cases signatures with no or one $b$-jet are considered. All results shown in the following are obtained assuming $pp$ collisions at $\sqrt{s} = 13\,\text{TeV}$, they employ `NNPDF40_nlo_as_01180` PDFs [70] and `Pythia 8` [71] is used to shower the events. Effects from hadronisation, underlying event modelling or QED effects in the PS are not included in our MC simulations.

### 4.1 Inclusive light dilepton final states

The simplest LHC searches for non-resonant DY phenomena (see for instance [2, 3]) use inclusive measurements of the high-mass dielectron or dimuon ($m_{\mu\mu}$) tail to set constraints on non-SM physics. In figure 3 we present our results for the LQ corrections to the $m_{\mu\mu}$ spectrum in inclusive $pp \to \mu^+\mu^-$ production adopting two benchmark choices for $Y_{b\mu}$ and $M_{\text{LQ}}$. All other LQ couplings are set to zero to obtain the results shown in the figure. The yellow and red curves in both plots correspond to the LQ distributions at the LO (LQ LO) and the NLO (LQ NLO) in QCD, respectively, while the green and blue histograms illustrate the impact of EW corrections (LQ EW) and the size of the interference effects between the LQ signal and the SM background (SM-LQ LO). From the lower panel of the left plot it is evident that for the choice $Y_{b\mu} = 2, M_{\text{LQ}} = 2\,\text{TeV}$ the NLO QCD effects play an important role in obtaining precise predictions as they amount compared to the tree-level LQ predictions to around 50% (80%) at $m_{\mu\mu} = 3\,\text{TeV}$ ($m_{\mu\mu} = 4\,\text{TeV}$). The corresponding numbers in the case of $Y_{b\mu} = 3, M_{\text{LQ}} = 3\,\text{TeV}$ are 25% and 40%. Higher-order EW corrections are far less important than the NLO QCD contributions at low invariant
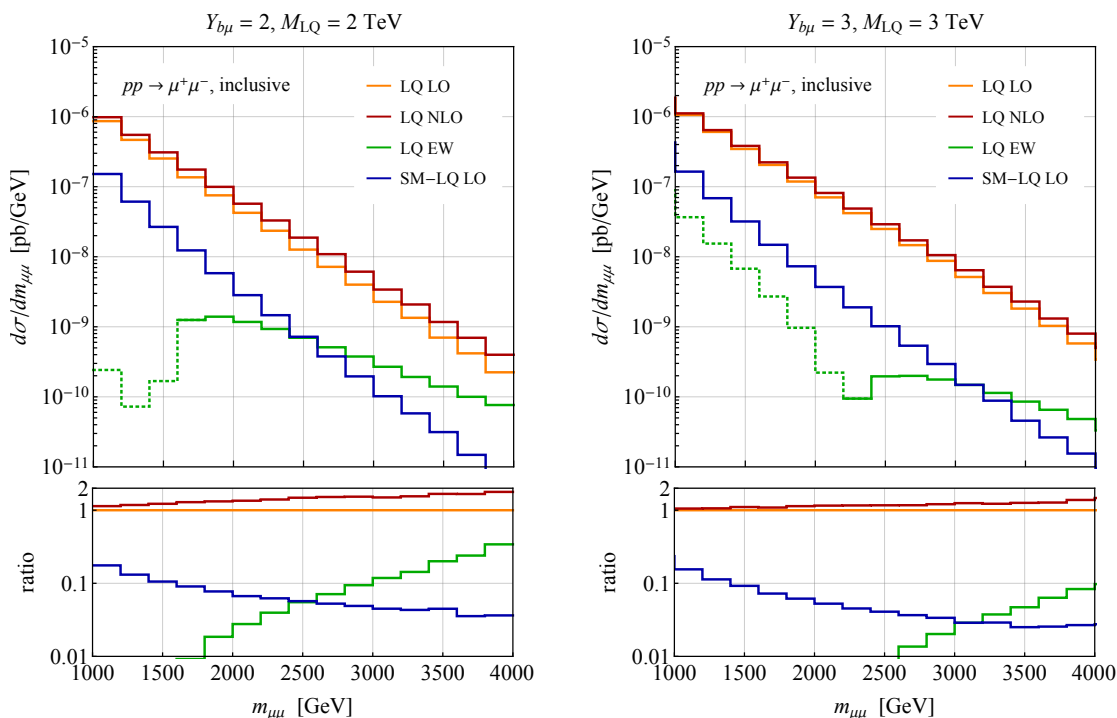
**Figure 3**. Inclusive $pp \to \mu^+\mu^-$ production cross sections as a function of $m_{\mu\mu}$. The left (right) plot shows the results for $Y_{b\mu} = 2, M_{\mathrm{LQ}} = 2\,\mathrm{TeV}$ ($Y_{b\mu} = 3, M_{\mathrm{LQ}} = 3\,\mathrm{TeV}$). The LQ couplings not specified in the headline of the plots are set to zero. The yellow and red curves correspond to the LQ distributions at the LO (LQ LO) and the NLO (LQ NLO) in QCD, respectively, while the green and blue histograms illustrate the impact of EW effects (LQ EW) and the size of the interference effects between the LQ signal and the SM background (SM-LQ LO). The parts of the green curves that are dotted correspond to negative EW contributions to the differential cross sections. The lower panels depict the ratios between the different LQ contributions and the relevant LQ LO distribution.

masses[2] but become relevant at high energies where they can lead to enhancements of the production rates of more than 30% for $Y_{b\mu} = 2, M_{\mathrm{LQ}} = 2\,\mathrm{TeV}$. This feature is well-known (cf. for example [72]) and due to the appearance of Sudakov logarithms of the form $\ln^2\left(m_{\mu\mu}^2/M_{\mathrm{LQ}}^2\right)$ which are associated to virtualites $q^2 \simeq m_{\mu\mu}^2$ that are much larger than the mass of the LQ entering the loop diagrams. The double-logarithmic behaviour also explains why for $Y_{b\mu} = 3, M_{\mathrm{LQ}} = 3\,\mathrm{TeV}$ the EW corrections are less pronounced than in the case of $Y_{b\mu} = 2, M_{\mathrm{LQ}} = 2\,\mathrm{TeV}$. Interference effects between the LQ signal and the SM background amount in both cases to approximately 5% in the high-mass tail of the $m_{\mu\mu}$ spectrum and are therefore only of minor importance.

The results shown in figure 3 already suggest that in existing LHC searches for non-resonant phenomena in DY distributions the phenomenological impact of EW and interference effects involving LQs is limited. To further illustrate this point we display in figure 4 the ratios between the individual LQ contributions and the inclusive DY SM background

---

[2]Below the LQ threshold the EW effects lead to a reduction of the differential DY cross section. This is indicated in figure 3 by the dotted green parts of the histograms.
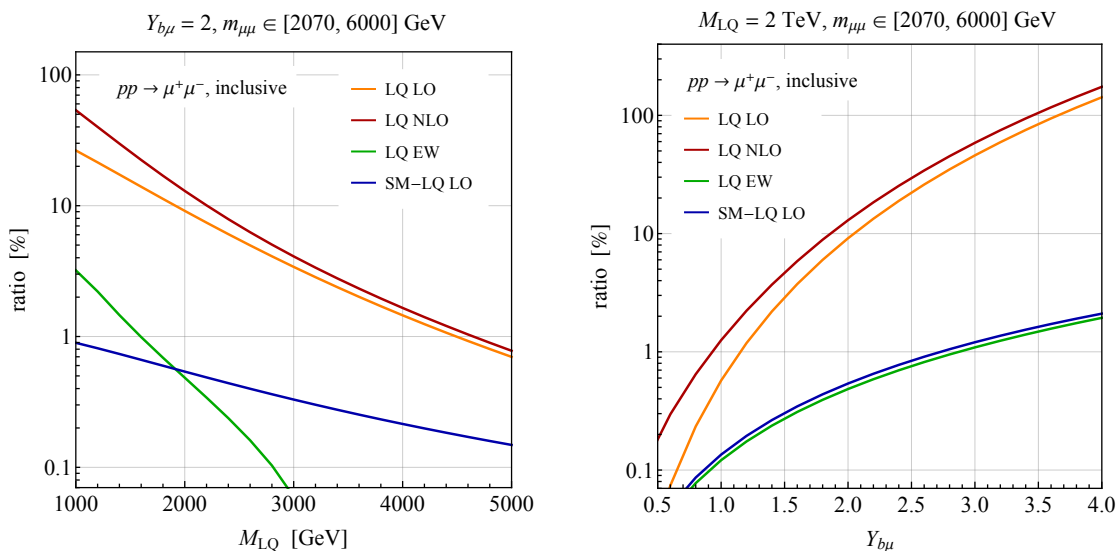
**Figure 4**. Ratios between the individual LQ corrections and the inclusive DY SM background calculated at the NLO in QCD. The shown results correspond to the fiducial region defined by $p_{T,\mu} > 30\,\text{GeV}$, $|\eta_\mu| < 2.5$ and $m_{\mu\mu} \in [2070, 6000]\,\text{GeV}$. The left (right) plot depicts the results as a function of $M_{\text{LQ}}$ ($Y_{b\mu}$) for fixed $Y_{b\mu} = 2$ ($M_{\text{LQ}} = 2\,\text{TeV}$). The colour coding and meaning of the different curves resembles those in figure 3. Additional details can be found in the main text.

in the fiducial region. The normalisation is calculated at the NLO in QCD and we select events that contain two opposite-sign same-flavour (OSSF) muons that are both required to have a transverse momentum of $p_{T,\mu} > 30\,\text{GeV}$ and a pseudorapidity of $|\eta_\mu| < 2.5$ and their invariant mass must fall into the range $m_{\mu\mu} \in [2070, 6000]\,\text{GeV}$. Detector efficiency corrections are not taken into account. Notice that this invariant mass window corresponds to the signal region (SR) used by ATLAS in their recent non-resonant dimuon analysis [2] assuming constructive signal-background interference. The left panel displays our results as a function of $M_{\text{LQ}}$ for fixed $Y_{b\mu} = 2$. From this plot one sees that the relative size of the NLO QCD corrections decreases for increasing LQ mass. Numerically, we find relative effects of around 100%, 20% and 10% at $M_{\text{LQ}} = 1\,\text{TeV}$, $M_{\text{LQ}} = 3\,\text{TeV}$ and $M_{\text{LQ}} = 5\,\text{TeV}$. This feature is readily understood by noting that the NLO QCD corrections related to $s$-channel single-LQ production followed by the decay of the LQ, cf. the left Feynman diagram in figure 2, decouple faster than the real and virtual corrections to the $t$-channel Born-level LQ contribution, cf. the middle and right graph in figure 1. Another property that is visible in the left panel is the strong suppression of the EW corrections for increasing $M_{\text{LQ}}$. This is related to the fact that for heavy LQs the enhancement of EW effects due to Sudakov double-logarithms is not at work in the considered SR. One furthermore observes that both the EW and the interference effects represent only subleading corrections in the mass window $m_{\mu\mu} \in [2070, 6000]\,\text{GeV}$, amounting to at most 3% and below 1%, respectively, in the shown LQ mass range.

The right panel in figure 4 depicts our ratio predictions as a function of $Y_{b\mu}$ setting the mass of the LQ to $M_{\text{LQ}} = 2\,\text{TeV}$. We see that the relative size of the NLO QCD corrections

decreases for increasing coupling strength. Compared to the tree-level LQ result the higher-order QCD effects amount to around 440%, 40% and 20% for $Y_{b\mu} = 0.5$, $Y_{b\mu} = 2$ and $Y_{b\mu} = 4$. This behaviour can be understood by realising that the squared amplitude of the $t$-channel Born-level contribution scales as $|Y_{b\mu}|^4$, while the resonant single-LQ production rate is proportional to $|Y_{b\mu}|^2$. One notices furthermore that the relative LQ EW and SM-LQ LO modifications both depend quadratically on $|Y_{b\mu}|$. One again sees that both the EW as well as the interference contributions are numerically subleading even for large couplings $Y_{b\mu}$ where they just reach the level of 1%.

### 4.2 Light dilepton final states with one $b$-jet

Inspired by the $b \to s\ell^+\ell^-$ anomalies also LHC searches for final states with two OSSF leptons and exactly one $b$-jet have been proposed [12] and recently performed by ATLAS [4]. In order to illustrate the improvement in sensitivity that is gained by targeting dilepton final states with additional $b$-jets, we show in figure 5 inclusive $pp \to \mu^+\mu^-$ cross sections as a function of $m_{\mu\mu}$ employing two different $b$-jet categories. We adopt the LQ parameter choices $Y_{b\mu} = 2$, $M_{\mathrm{LQ}} = 2\,\mathrm{TeV}$ and consider $139\,\mathrm{fb}^{-1}$ of integrated luminosity under LHC Run II conditions. Following the study [4] events are selected with two OSSF muons that are both required to satisfy $p_{T,\mu} > 30\,\mathrm{GeV}$ and $|\eta_\mu| < 2.5$. Jets are reconstructed using the anti-$k_t$ algorithm [73] with radius parameter $R = 0.4$, as implemented in `FastJet` [74], and need to fulfil $p_{T,j} > 30\,\mathrm{GeV}$ and $|\eta_j| < 2.5$. Jets originating from the hadronisation of a bottom or anti-bottom quark are identified (i.e. $b$-tagged) adopting the performance of the ATLAS $b$-tagging algorithm described in [75]. For the analyses performed in this subsection, a $b$-tagging working point is chosen that yields a $b$-tagging efficiency of 77% and a light-flavour jet rejection of 110. Detector effects are simulated by applying reconstruction and identification efficiency factors tuned to mimic the performance of the ATLAS detector. In particular, muon candidates must fulfil the ATLAS quality selection criteria optimised for high-$p_T$ performance [76, 77]. The corresponding reconstruction and identification efficiency amount to around 75% in the phase-space region of interest. Our analysis is implemented into `MadAnalysis 5` [78] and employs `Delphes 3` [79] as a fast detector simulator. Applying our MC chain to the SM NLO prediction obtained with the `POWHEG-BOX`, we are able reproduce the SM DY background postfit $m_{\mu\mu}$ distribution in the SR provided by ATLAS in [4] at the level of 10%. This comparison represents a non-trivial cross-check of our analysis.

In the left panel of figure 5 our results for the inclusive DY dimuon cross section with no $b$-tagged jet ($b$-veto) are presented. The black, yellow and red histogram display the SM results obtained at NLO in QCD (SM NLO), the LQ LO and the LQ NLO predictions, respectively. The size of EW and interference effects is not shown in the figure because these corrections are both very small. One observes that in the $b$-veto category the LQ contributions to the differential rate amount to corrections of a few percent only, and that NLO QCD corrections modifying the LO LQ spectrum by around 10% to 20% in the shown $m_{\mu\mu}$ range. Requiring one $b$-jet ($b$-tag) in addition to the two OSSF muons changes the picture radically. This is illustrated on the right-hand side in figure 5. In fact, the requirement of an additional $b$-jet reduces the SM background by roughly a factor of
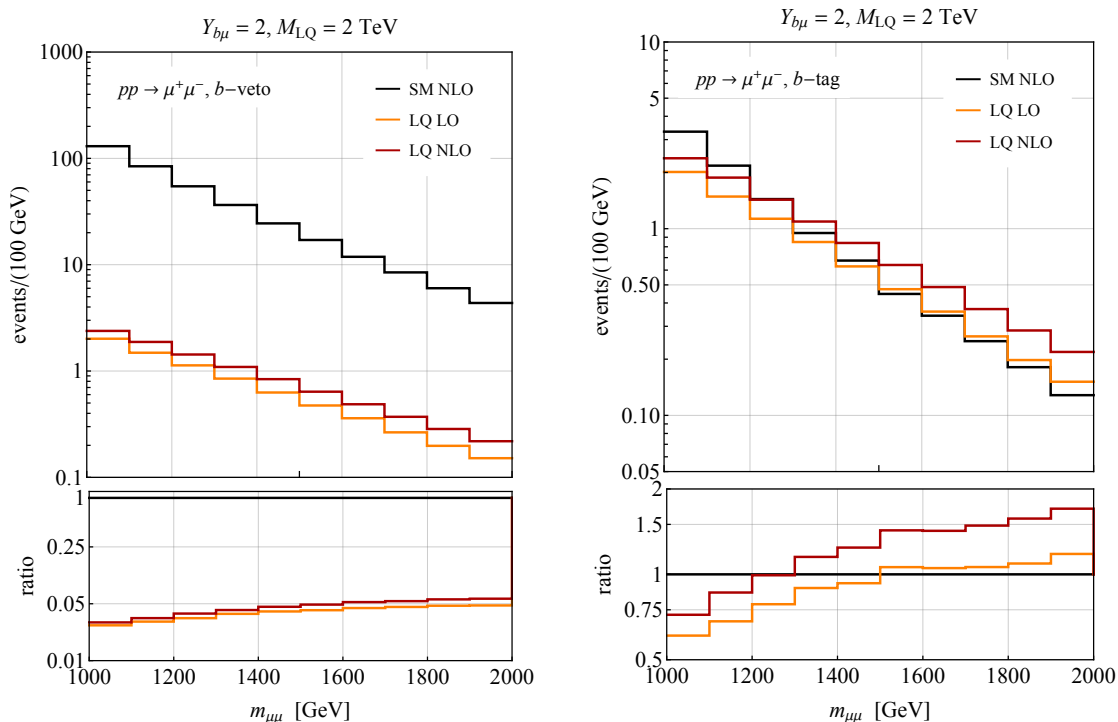
**Figure 5**. Inclusive $pp \to \mu^+\mu^-$ production cross sections as a function of $m_{\mu\mu}$ for two different $b$-jet categories. The left (right) plot shows the results for $Y_{b\mu} = 2, M_{\mathrm{LQ}} = 2\,\mathrm{TeV}$ imposing a $b$-veto ($b$-tag). The black, yellow and red curves correspond to the SM results obtained at NLO in QCD (SM NLO), the LQ LO and the LQ NLO predictions, respectively. All results assume an integrated luminosity of $139\,\mathrm{fb}^{-1}$. The lower panels display the ratios between the different LQ contributions and the corresponding SM NLO spectrum. Further details can be found in the main text.

35 largely independent of $m_{\mu\mu}$, while the $b$-jet requirement has an effect of around $-60\%$ ($-15\%$) on the signal strength in the considered LQ realisation at $m_{\mu\mu} = 1\,\mathrm{TeV}$ ($m_{\mu\mu} = 2\,\mathrm{TeV}$). It is also visible that the size of the NLO QCD corrections to the LQ signal is larger in the case of the $b$-tag than the $b$-veto category, exceeding $25\%$ above approximately $m_{\mu\mu} = 1.5\,\mathrm{TeV}$. This feature is explained by noting that NLO QCD contributions of the form $gb \to \tilde{S}_1\mu^-$ with $\tilde{S}_1 \to b\mu^+$, cf. the left diagram in figure 2, will mostly contribute to the $b$-tag category. Similar statements apply to channels like $gb \to \mu^+\mu^- b$ where the anti-bottom quark that partakes in the $t$-channel LQ process $b\bar{b} \to \mu^+\mu^-$ arises from splitting of an initial-state gluon. Notice however that while the latter type of corrections can be partly captured by a PS when applied to the LO matrix elements, this is not the case for the former contribution associated to resonant single-LQ production. In order to achieve an accurate exclusive description of DY dilepton processes in LQ models involving heavy-flavoured jets, NLO+PS predictions as provided in our work are therefore called for.

### 4.3 Heavy dilepton final states with and without a $b$-jet

Searches for signatures involving tau pairs in the final state such as those performed at LHC Run II [1, 6] are known [7, 11, 15–18, 22] to provide strong constraints on LQ models

that address the $b \to c\ell\nu$ anomalies. In the following we will consider the recent CMS search [6] for $\tau^+\tau^-$ final states with both taus decaying to hadrons ($\tau_{\mathrm{h}}^{\pm}$) as an example to illustrate the role that additional $b$-jets play in analyses of this kind. To distinguish hadronic $\tau$ candidates from jets originating from the hadronisation of quarks and gluons, and from electrons or muons the $\tau$-tagger described in [80] is employed. The used working points have an efficiency of approximately 50%, 70% and 70% for identification in the case of jets, electrons and muons, respectively. The corresponding rejection factors are around 230, 20, and 770. Both hadronic $\tau$ candidates are required to have $p_{T,\tau} > 40\,\mathrm{GeV}$ and $|\eta_\tau| < 2.1$, and the angular distance between them must be greater than $\Delta R_{\tau\tau} = 0.3$ in the pseudorapidity-azimuth space. Jets are clustered using the anti-$k_t$ algorithm with radius $R = 0.4$. Jets with $p_{T,j} > 30\,\mathrm{GeV}$ and $|\eta_j| < 4.7$ and $b$-jets with $p_{T,b} > 20\,\mathrm{GeV}$ and $|\eta_b| < 2.5$ are selected. To identify $b$-jets we employ the CMS $b$-tagging efficiencies stated in [81, 82]. The used $b$-tagging working point yields a $b$-tagging efficiency of around 80% and a light-flavour jet rejection in the ballpark of 100. `MadAnalysis 5` in combination with `Delphes 3` is again used to analyse the events and to simulate the detector effects. We have verified that applying our analysis to the SM NLO DY prediction, we are able reproduce the SM DY background as given in [6] to within around 30%.

To discriminate between signal and background, we consider the distributions of the total transverse mass defined as [83]

$$m_T^{\mathrm{tot}} = \sqrt{m_T^2(\vec{p}_T^{\,\tau_1}, \vec{p}_T^{\,\tau_2}) + m_T^2(\vec{p}_T^{\,\tau_1}, \vec{p}_T^{\,\mathrm{miss}}) + m_T^2(\vec{p}_T^{\,\tau_2}, \vec{p}_T^{\,\mathrm{miss}})} \,, \tag{4.1}$$

where $\tau_1$ ($\tau_2$) refers to the first (second) hadronic $\tau$ candidate and $\vec{p}_T^{\,\tau_1}$, $\vec{p}_T^{\,\tau_2}$ and $\vec{p}_T^{\,\mathrm{miss}}$ are the vectors with magnitude $p_{T,\tau_1}$, $p_{T,\tau_2}$ and $E_{T,\mathrm{miss}}$. Here $E_{T,\mathrm{miss}}$ denotes the missing transverse energy constructed from the transverse momenta of all the neutrinos in the event. The transverse mass of two transverse momenta $p_{T,i}$ and $p_{T,j}$ entering (4.1) is given by

$$m_T(\vec{p}_T^{\,i}, \vec{p}_T^{\,j}) = \sqrt{2 p_{T,i} p_{T,j} \left(1 - \cos \Delta\phi\right)} \,, \tag{4.2}$$

where $\Delta\phi$ is the azimuthal angular difference between the vectors $\vec{p}_T^{\,i}$ and $\vec{p}_T^{\,j}$.

In the two panels of figure 6 we compare the $m_T^{\mathrm{tot}}$ distributions within the SM and in the benchmark LQ model for the parameter choices $Y_{b\tau} = 2$, $M_{\mathrm{LQ}} = 2\,\mathrm{TeV}$. The left (right) plot shows the results for the no $b$-tag ($b$-tag) category in the $\tau_{\mathrm{h}}^+ \tau_{\mathrm{h}}^-$ final state. The black curves represent the SM expectations of the DY background taken from [6], while the yellow and red histograms are the LQ LO and LQ NLO predictions obtained using our `POWHEG-BOX` implementation. All results assume $138\,\mathrm{fb}^{-1}$ of $pp$ data collected at $\sqrt{s} = 13\,\mathrm{TeV}$. It is evident from the lower left panel that in the no $b$-tag category the NLO LQ contribution amounts to a relative correction of only about 10% compared to the SM DY background for $m_T^{\mathrm{tot}} > 1300\,\mathrm{GeV}$. In the case of the $b$-tag category, one instead observes from the lower right panel that in the highest $m_T^{\mathrm{tot}}$ bin with $m_T^{\mathrm{tot}} > 900\,\mathrm{GeV}$ the NLO LQ signal constitutes almost 110% of the SM DY background. This again demonstrates that for third-generation scalar LQs the sensitivity of DY searches notably improves by demanding additional $b$-jet activity. Notice that the NLO QCD effects enhance the LO LQ predictions in the no $b$-tag ($b$-tag) category by approximately 40% (30%) in the highest $m_T^{\mathrm{tot}}$ bin, making higher-order
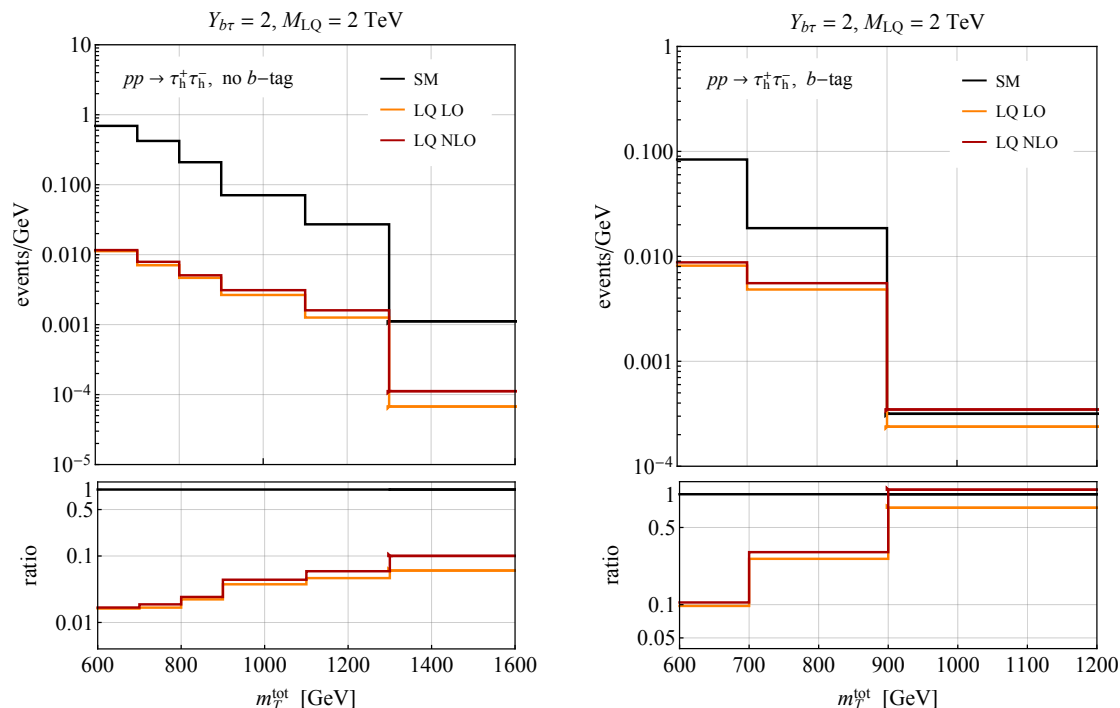
**Figure 6**. Distributions of $m_T^{tot}$ in the no $b$-tag (left panel) and the $b$-tag (right panel) categories in the $\tau_h^+ \tau_h^-$ final state. The black curves correspond to the SM expectations of the DY background provided by CMS in the search [6] which is based on $138 \, \text{fb}^{-1}$ of LHC Run II data The yellow and red curves instead represent the LQ LO and LQ NLO results assuming $Y_{b\tau} = 2, M_{\text{LQ}} = 2 \, \text{TeV}$. The definition of the SRs and other experimental details are given in the main text.

QCD effects phenomenologically relevant if one wants to obtain precise predictions. On the other hand, EW and interference effects are both insignificant in the tail of the $m_T^{tot}$ distribution and are therefore not shown in the figure.

## 5 Exclusion limits

On the basis of the search strategies detailed in section 4, we will now derive 95% confidence level (CL) constraints on the $M_{\text{LQ}}$–$Y_{b\mu}$ and $M_{\text{LQ}}$–$Y_{b\tau}$ planes using the latest LHC dilepton analyses performed at LHC Run II. Additional exclusion limits on the parameter space of second-generation scalar LQs can be found in appendix A. In the left panel of figure 7 we show the 95% C.L. limits on the $M_{\text{LQ}}$–$Y_{b\mu}$ parameter space. The yellow, red and green bounds arise from the inclusive DY search [2] and the DY analysis [4] in the $b$-veto and $b$-tag category, respectively. All exclusions are based on NLO+PS predictions obtained with the POWHEG-BOX. The hatched grey region of parameter space with $M_{\text{LQ}} < 1720 \, \text{GeV}$ is finally excluded by the search [84] for QCD pair production of scalar LQs. The displayed exclusions are derived directly from the observed model-independent upper 95% C.L. limits on the visible cross section times branching ratio provided in [2, 4]. From the shown results it is evident that the search strategy that requires besides two OSSF
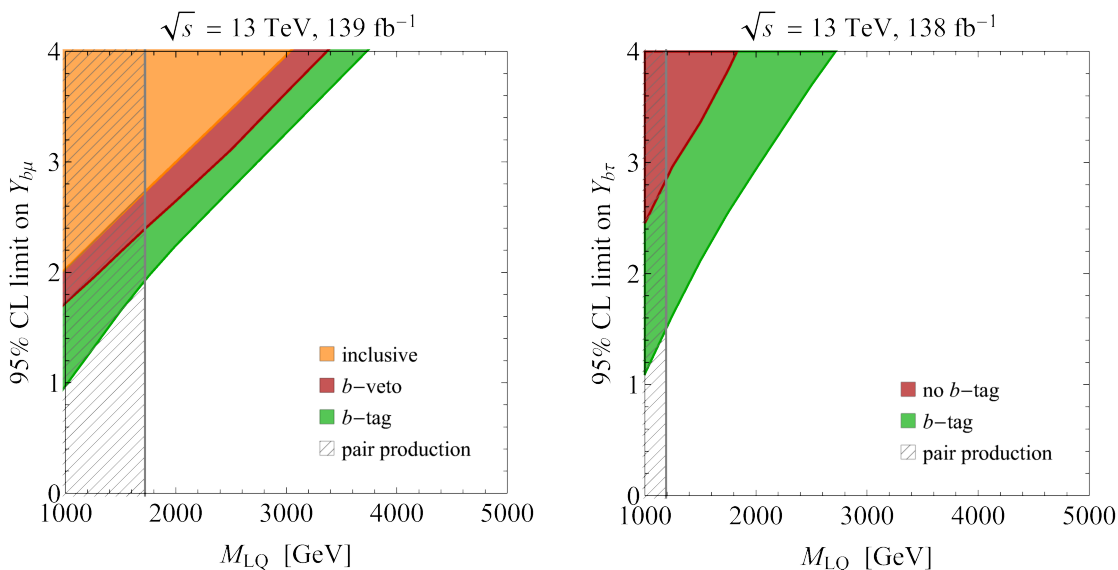
**Figure 7**. Left: comparison of the 95% C.L. constraints on the $M_{\text{LQ}}$–$Y_{b\mu}$ plane following from different search strategies at LHC Run II. The yellow, red and green limit corresponds to the inclusive DY search [2] and the DY analysis [4] in the $b$-veto and $b$-tag category, respectively. The hatched grey parameter space is instead excluded by the search [84] for strong LQ pair production. Right: comparison of the 95% C.L. constraints on the $M_{\text{LQ}}$–$Y_{b\tau}$ plane that arise from the LHC Run II double hadronic ditau analysis [6]. The green (red) exclusion corresponds to the no $b$-tag ($b$-tag) category of the latter search, while the hatched grey parameter space is excluded by strong pair production of third-generation LQs [85]. Consult the main text for additional explanations.

muons a $b$-tag leads to the best exclusion. As explained in section 4.2 this is to be expected because the requirement of an additional $b$-tagged jet leads to a strong reduction of the signal-to-background ratio. Notice also that for $M_{\text{LQ}} \lesssim 1.7\,\text{TeV}$ the exclusion contour starts to deviate from its linear behaviour. This is a consequence of the contribution associated to single-LQ production with subsequent decay of the LQ, cf. the left diagram in figure 2, scaling as $|Y_{b\mu}|^2$ compared to the $|Y_{b\mu}|^4$ dependence of the squared amplitude of the $t$-channel Born-level LQ contribution. Another interesting feature of the results shown on the left-hand side in figure 7 is that the $b$-veto search performs better than the inclusive search strategy. This feature is related to the fact that the SR with $m_{\mu\mu} \in [2070, 6000]\,\text{GeV}$ employed in [2] is not optimised for the LQ signals studied here. Using the model-independent limits as a function of the minimum dimuon invariant mass $m_{\mu\mu}^{\text{min}}$, i.e. $m_{\mu\mu} > m_{\mu\mu}^{\text{min}}$, presented in [4] that covers lower values of $m_{\mu\mu}^{\text{min}}$ instead allows for such an optimisation and therefore leads to a stronger bound.

In the right panel of figure 7 we finally display the 95% C.L. exclusion bounds in the $M_{\text{LQ}}$–$Y_{b\tau}$ plane that follow from the two $b$-jet categories considered in the $\tau_{\text{h}}^+\tau_{\text{h}}^-$ search [6]. The green and red exclusion corresponds to the no $b$-tag and the $b$-tag category of this analysis, respectively, while the parameter space excluded by strong pair production of third-generation LQs [85] is indicated by the hatched grey vertical band. This search excludes $M_{\text{LQ}} < 1190\,\text{GeV}$ at 95% C.L. The significance of the individual $b$-jet categories of the search [6] is calculated as a Poisson ratio of likelihoods modified to incorporate

systematic uncertainties on the background as Gaussian constraints [86]. Our statistical analysis includes the six (three) highest $m_T^{\rm tot}$ bins in the case of the no $b$-tag ($b$-tag) category. As for the exclusion limits on the coupling $Y_{b\mu}$, one observes that the bound on $Y_{b\tau}$ that follows from the search with a $b$-tag is more stringent than the one that derives from a strategy that vetos $b$-jets. Notice lastly that as an effect of single-LQ production the slope of the exclusion arising from the $b$-tag category changes at around $M_{\rm LQ} = 1.2\,{\rm TeV}$, although this effect is less visible in the case of the coupling $Y_{b\tau}$ than for $Y_{b\mu}$.

## 6  Conclusions and outlook

In this article we have refined the theoretical description of DY dilepton production in scalar LQ models. To achieve this goal we have calculated the NLO QCD corrections to $pp \to \ell^+\ell^-$ production. The actual computation involves the evaluation of the real and virtual corrections to the $t$-channel Born-level contribution and the calculation of resonant single-LQ production followed by the decay of the LQ. Besides QCD corrections we have also considered the impact of virtual EW corrections and studied the size of interference effects between the LQ signal and the DY SM background. These fixed-order predictions are consistently matched to a PS employing the POWHEG method, which makes it possible to obtain a realistic exclusive description of DY dilepton processes in scalar LQ models at the level of hadronic events. Our POWHEG implementation allows in particular to generate events with one additional parton from the matrix element calculation without the introduction of a merging or matching scale. Since we believe that the presented MC generator should prove useful for everyone interested in comparing accurate theory predictions to LHC data, we will make the relevant codes to simulate NLO+PS events for the $pp \to \ell^+\ell^-$ process in scalar LQ models of the form (2.1) publicly available on the POWHEG-BOX web page [87].

While our MC implementation can generate dilepton DY predictions for all couplings entering the simplified LQ Lagrangian (2.1), we have confined ourselves in the main part of this work to the case of $b \to \mu$ and $b \to \tau$ flavour transitions in our phenomenological analyses. The focus on these two cases is firstly motivated by the observation that in scalar LQ models that offer an explanation of the anomalies in semileptonic $B$ decays, the Yukawa entries $Y_{b\mu}$ and $Y_{b\tau}$ are necessarily the largest couplings. Second, since for $Y_{b\mu} \neq 0$ ($Y_{b\tau} \neq 0$) DY dimuon (ditau) production is induced at the tree level via bottom-quark fusion, initial-state radiation will always lead to a certain amount of $b$-jet activity. In such cases, devising search strategies with different $b$-jet categories is expected to help improve the LHC sensitivity. To illustrate the latter point, we have performed recasts of the existing LHC Run II searches [2, 4, 6] that employ around $140\,{\rm fb}^{-1}$ of $pp$ data collected at $\sqrt{s} = 13\,{\rm TeV}$. In particular, we have derived the limits on the couplings $Y_{b\mu}$ and $Y_{b\tau}$ and masses of third-generation scalar LQs from the relevant LHC searches, considering signatures with no or one $b$-jet. We found that the exclusive strategies that require the presence of an additional $b$-tagged jet always perform better than inclusive searches or those that veto $b$-jets. The improvement in sensitivity is particularly important in the case of the $pp \to \mu^+\mu^-$ searches because the top and multijet background contributions to the $b$-tagged sample are compared to $pp \to \tau^+\tau^-$ less relevant. Although we have presented in our work

only results for $pp \to \mu^+\mu^-$, the latter statement applies to $pp \to e^+e^-$ production as well. For completeness we provide the constraints on the parameter space of second-generation scalar LQs that arise from DY dilepton production in the supplementary material that can be found in appendix A.

Let us finally add that measurements of the DY forward-backward asymmetry ($A_{\rm FB}$) at high dilepton invariant masses such as [5] might also be used to set limits on the presence of LQs and their interactions [8]. The forward (backward) DY cross section thereby includes all events with $\cos\theta > 0$ ($\cos\theta < 0$) where $\theta$ denotes the angle between the incoming quark and the outgoing negatively charged lepton in the Collins-Soper frame [88]. At a *pp* collider like the LHC this however means that non-zero $A_{\rm FB}$ values can only arise from the valence quarks but not the sea quarks. Since we have discussed in this work only LQ processes initiated by heavy-quark fusion, we have therefore not studied the constraints that arise from $A_{\rm FB}$. We however emphasise that our MC implementation is able to calculate the first-generation scalar LQ contributions to $A_{\rm FB}$ including NLO QCD, EW and interference effects.

## Acknowledgments

## A  Supplementary material

Employing the search strategies detailed already in section 4, we present in this appendix the 95% C.L. exclusion limits on the $M_{\rm LQ}$–$Y_{s\mu}$ and $M_{\rm LQ}$–$Y_{c\tau}$ planes using the latest LHC dilepton analyses performed at LHC Run II. Such limits are of interest because besides the Yukawa entries $Y_{b\mu}$ and $Y_{b\tau}$ discussed in section 5 also $Y_{s\mu}$ and $Y_{c\tau}$ enter the predictions for $b \to s\mu^+\mu^-$ and $b \to c\tau\nu$ in scalar LQ models. All results displayed below are based on NLO+PS predictions obtained with our dedicated `POWHEG-BOX` implementation of the interaction Lagrangian (2.1). Our statistical analyses employ the methodologies that have been briefly described in section 5.

The yellow and red bound shown on the left-hand side of figure 8 corresponds to the inclusive search [2] and the analysis [4] imposing a *b*-veto. For comparison, we also display the parameter space with $M_{\rm LQ} < 1730\,{\rm GeV}$ that is excluded by the search [84] for strong LQ pair production as a hatched grey vertical band. Like in the case of the coupling $Y_{b\mu}$, cf. the left panel in figure 7, one sees that the exclusion following from the *b*-veto search surpasses the limit that derives from the inclusive analysis. The reason is again that by choosing $m_{\mu\mu}^{\rm min}$ appropriately the sensitivity of the *b*-veto search can be improved
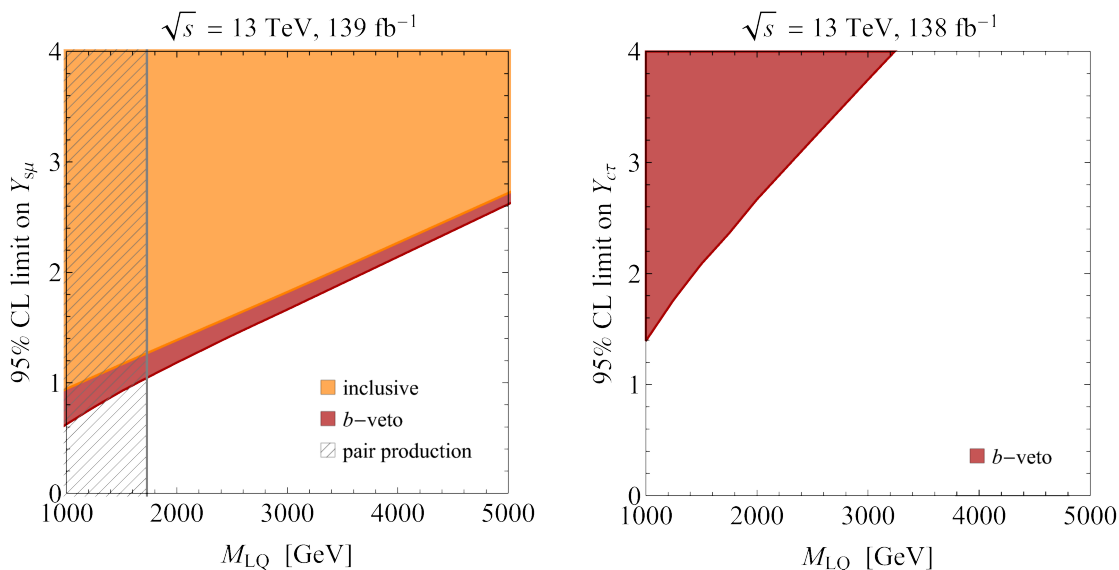
**Figure 8**. As figure 7 but for the couplings $Y_{s\mu}$ (left panel) and $Y_{c\tau}$ (right panel). See main text for further explanations.

over that of the inclusive analysis which uses a fixed and rather high value of $m_{\mu\mu}^{\min}$. On the right in figure 8 we finally present the 95% C.L. exclusion limit on the $M_{\rm LQ}$–$Y_{c\tau}$ plane that originates from a recast of the search with a $b$-veto that has been performed in the publication [4]. Notice that neither ATLAS nor CMS has searched for pairs of scalar LQs decaying into light-flavour quarks and tau leptons. This explains why no bound from QCD LQ pair production included in the right panel of figure 8. Finally, we add that a DY ditau search that requires a $c$-tag is likely to allow to strengthen the exclusion bounds on the $M_{\rm LQ}$–$Y_{c\tau}$ plane compared to the limits presented in this appendix. Given the latest advances in tagging charm quarks at the LHC [75, 90] and the successful applications of these techniques in the recent searches for the SM Higgs boson decaying to charm-quark pairs [91, 92], we believe that OSSF dilepton searches with the requirement of an additional $c$-jet would be an interesting addition to the exotics search canon of both the ATLAS and CMS collaborations.

**Open Access.** This article is distributed under the terms of the Creative Commons Attribution License ([CC-BY 4.0](#)), which permits any use, distribution and reproduction in any medium, provided the original author(s) and source are credited. SCOAP$^3$ supports the goals of the International Year of Basic Sciences for Sustainable Development.

## References

[1] ATLAS collaboration, *Search for heavy Higgs bosons decaying into two tau leptons with the ATLAS detector using pp collisions at $\sqrt{s} = 13$ TeV*, *Phys. Rev. Lett.* **125** (2020) 051801 [arXiv:2002.12223] [INSPIRE].

[2] ATLAS collaboration, *Search for new non-resonant phenomena in high-mass dilepton final states with the ATLAS detector*, *JHEP* **11** (2020) 005 [*Erratum JHEP* **04** (2021) 142] [arXiv:2006.12946] [INSPIRE].

[3] CMS collaboration, *Search for resonant and nonresonant new phenomena in high-mass dilepton final states at $\sqrt{s} = 13$ TeV*, *JHEP* **07** (2021) 208 [arXiv:2103.02708] [INSPIRE].

[4] ATLAS collaboration, *Search for New Phenomena in Final States with Two Leptons and One or No b-Tagged Jets at $\sqrt{s} = 13$ TeV Using the ATLAS Detector*, *Phys. Rev. Lett.* **127** (2021) 141801 [arXiv:2105.13847] [INSPIRE].

[5] CMS collaboration, *Measurement of the Drell-Yan forward-backward asymmetry at high dilepton masses in proton-proton collisions at $\sqrt{s} = 13$ TeV*, *JHEP* **08** (2022) 063 [arXiv:2202.12327] [INSPIRE].

[6] CMS collaboration, *Searches for additional Higgs bosons and vector leptoquarks in $\tau\tau$ final states in proton-proton collisions at $\sqrt{s} = 13$ TeV*, CERN, Geneva, Switzerland (2022) [CMS-PAS-HIG-21-001].

[7] D.A. Faroughy, A. Greljo and J.F. Kamenik, *Confronting lepton flavor universality violation in B decays with high-$p_T$ tau lepton searches at LHC*, *Phys. Lett. B* **764** (2017) 126 [arXiv:1609.07138] [INSPIRE].

[8] N. Raj, *Anticipating nonresonant new physics in dilepton angular spectra at the LHC*, *Phys. Rev. D* **95** (2017) 015011 [arXiv:1610.03795] [INSPIRE].

[9] A. Greljo and D. Marzocca, *High-$p_T$ dilepton tails and flavor physics*, *Eur. Phys. J. C* **77** (2017) 548 [arXiv:1704.09015] [INSPIRE].

[10] B.C. Allanach, B. Gripaios and T. You, *The case for future hadron colliders from $B \to K^{(*)}\mu^+\mu^-$ decays*, *JHEP* **03** (2018) 021 [arXiv:1710.06363] [INSPIRE].

[11] I. Doršner and A. Greljo, *Leptoquark toolbox for precision collider studies*, *JHEP* **05** (2018) 126 [arXiv:1801.07641] [INSPIRE].

[12] Y. Afik, J. Cohen, E. Gozani, E. Kajomovitz and Y. Rozen, *Establishing a Search for $b \to s\ell^+\ell^-$ Anomalies at the LHC*, *JHEP* **08** (2018) 056 [arXiv:1805.11402] [INSPIRE].

[13] S. Bansal, R.M. Capdevilla, A. Delgado, C. Kolda, A. Martin and N. Raj, *Hunting leptoquarks in monolepton searches*, *Phys. Rev. D* **98** (2018) 015037 [arXiv:1806.02370] [INSPIRE].

[14] B.C. Allanach, T. Corbett, M.J. Dolan and T. You, *Hadron collider sensitivity to fat flavourful Z's for $R_{K^{(*)}}$*, *JHEP* **03** (2019) 137 [arXiv:1810.02166] [INSPIRE].

[15] M. Schmaltz and Y.-M. Zhong, *The leptoquark Hunter's guide: large coupling*, *JHEP* **01** (2019) 132 [arXiv:1810.10017] [INSPIRE].

[16] T. Mandal, S. Mitra and S. Raz, *$R_{D^{(*)}}$ motivated $\mathcal{S}_1$ leptoquark scenarios: Impact of interference on the exclusion limits from LHC data*, *Phys. Rev. D* **99** (2019) 055028 [arXiv:1811.03561] [INSPIRE].

[17] M.J. Baker, J. Fuentes-Martín, G. Isidori and M. König, *High-$p_T$ signatures in vector-leptoquark models*, *Eur. Phys. J. C* **79** (2019) 334 [arXiv:1901.10480] [INSPIRE].

[18] D. Choudhury, N. Kumar and A. Kundu, *Search for an opposite sign muon-tau pair and a b-jet at the LHC in the context of flavor anomalies*, *Phys. Rev. D* **100** (2019) 075001 [arXiv:1905.07982] [INSPIRE].

[19] A. Angelescu, D.A. Faroughy and O. Sumensari, *Lepton Flavor Violation and Dilepton Tails at the LHC*, *Eur. Phys. J. C* **80** (2020) 641 [arXiv:2002.05684] [INSPIRE].

[20] A. Bhaskar, D. Das, T. Mandal, S. Mitra and C. Neeraj, *Precise limits on the charge-2/3 $U_1$ vector leptoquark*, *Phys. Rev. D* **104** (2021) 035016 [arXiv:2101.12069] [INSPIRE].

[21] A. Crivellin, C.A. Manzari and M. Montull, *Correlating nonresonant di-electron searches at the LHC to the Cabibbo-angle anomaly and lepton flavor universality violation*, *Phys. Rev. D* **104** (2021) 115016 [arXiv:2103.12003] [INSPIRE].

[22] C. Cornella, D.A. Faroughy, J. Fuentes-Martin, G. Isidori and M. Neubert, *Reading the footprints of the B-meson flavor anomalies*, *JHEP* **08** (2021) 050 [arXiv:2103.16558] [INSPIRE].

[23] A. Crivellin, D. Müller and L. Schnell, *Combined constraints on first generation leptoquarks*, *Phys. Rev. D* **103** (2021) 115023 [*Addendum ibid.* **104** (2021) 055020] [arXiv:2104.06417] [INSPIRE].

[24] A. Crivellin, M. Hoferichter, M. Kirk, C.A. Manzari and L. Schnell, *First-generation new physics in simplified models: from low-energy parity violation to the LHC*, *JHEP* **10** (2021) 221 [arXiv:2107.13569] [INSPIRE].

[25] B. Garland, S. Jäger, C.K. Khosa and S. Kvedaraitė, *Probing B anomalies via dimuon tails at a future collider*, *Phys. Rev. D* **105** (2022) 115017 [arXiv:2112.05127] [INSPIRE].

[26] A. Crivellin, B. Fuks and L. Schnell, *Explaining the hints for lepton flavour universality violation with three $S_2$ leptoquark generations*, *JHEP* **06** (2022) 169 [arXiv:2203.10111] [INSPIRE].

[27] A. Azatov, F. Garosi, A. Greljo, D. Marzocca, J. Salko and S. Trifinopoulos, *New physics in $b \to s\mu\mu$: FCC-hh or a muon collider?*, *JHEP* **10** (2022) 149 [arXiv:2205.13552] [INSPIRE].

[28] BaBar collaboration, *Evidence for an excess of $\bar{B} \to D^{(*)}\tau^-\bar{\nu}_\tau$ decays*, *Phys. Rev. Lett.* **109** (2012) 101802 [arXiv:1205.5442] [INSPIRE].

[29] BaBar collaboration, *Measurement of an Excess of $\bar{B} \to D^{(*)}\tau^-\bar{\nu}_\tau$ Decays and Implications for Charged Higgs Bosons*, *Phys. Rev. D* **88** (2013) 072012 [arXiv:1303.0571] [INSPIRE].

[30] LHCb collaboration, *Measurement of the ratio of branching fractions $\mathcal{B}(\bar{B}^0 \to D^{*+}\tau^-\bar{\nu}_\tau)/\mathcal{B}(\bar{B}^0 \to D^{*+}\mu^-\bar{\nu}_\mu)$*, *Phys. Rev. Lett.* **115** (2015) 111803 [*Erratum ibid.* **115** (2015) 159901] [arXiv:1506.08614] [INSPIRE].

[31] LHCb collaboration, *Measurement of the ratio of the $B^0 \to D^{*-}\tau^+\nu_\tau$ and $B^0 \to D^{*-}\mu^+\nu_\mu$ branching fractions using three-prong $\tau$-lepton decays*, *Phys. Rev. Lett.* **120** (2018) 171802 [arXiv:1708.08856] [INSPIRE].

[32] LHCb collaboration, *Test of Lepton Flavor Universality by the measurement of the $B^0 \to D^{*-}\tau^+\nu_\tau$ branching fraction using three-prong $\tau$ decays*, *Phys. Rev. D* **97** (2018) 072013 [arXiv:1711.02505] [INSPIRE].

[33] Belle collaboration, *Measurement of $\mathcal{R}(D)$ and $\mathcal{R}(D^*)$ with a semileptonic tagging method*, arXiv:1904.08794 [INSPIRE].

[34] LHCb collaboration, *Test of lepton universality with $B^0 \to K^{*0}\ell^+\ell^-$ decays*, *JHEP* **08** (2017) 055 [arXiv:1705.05802] [INSPIRE].

[35] LHCb collaboration, *Search for lepton-universality violation in $B^+ \to K^+\ell^+\ell^-$ decays*, *Phys. Rev. Lett.* **122** (2019) 191801 [arXiv:1903.09252] [INSPIRE].

[36] Belle collaboration, *Test of Lepton-Flavor Universality in $B \to K^*\ell^+\ell^-$ Decays at Belle*, *Phys. Rev. Lett.* **126** (2021) 161801 [arXiv:1904.02440] [INSPIRE].

[37] BELLE collaboration, *Test of lepton flavor universality and search for lepton flavor violation in $B \to K\ell\ell$ decays*, *JHEP* **03** (2021) 105 [arXiv:1908.01848] [INSPIRE].

[38] LHCb collaboration, *Test of lepton universality in beauty-quark decays*, *Nature Phys.* **18** (2022) 277 [arXiv:2103.11769] [INSPIRE].

[39] W. Altmannshofer, P.S. Bhupal Dev and A. Soni, $R_{D^{(*)}}$ *anomaly: A possible hint for natural supersymmetry with R-parity violation*, *Phys. Rev. D* **96** (2017) 095010 [arXiv:1704.06659] [INSPIRE].

[40] S. Iguro and K. Tobe, $R(D^{(*)})$ *in a general two Higgs doublet model*, *Nucl. Phys. B* **925** (2017) 560 [arXiv:1708.06176] [INSPIRE].

[41] M. Abdullah, J. Calle, B. Dutta, A. Flórez and D. Restrepo, *Probing a simplified, $W'$ model of $R(D^{(*)})$ anomalies using b-tags, $\tau$ leptons and missing energy*, *Phys. Rev. D* **98** (2018) 055016 [arXiv:1805.01869] [INSPIRE].

[42] D. Marzocca, U. Min and M. Son, *Bottom-Flavored Mono-Tau Tails at the LHC*, *JHEP* **12** (2020) 035 [arXiv:2008.07541] [INSPIRE].

[43] M. Endo, S. Iguro, T. Kitahara, M. Takeuchi and R. Watanabe, *Non-resonant new physics search at the LHC for the $b \to c\tau\nu$ anomalies*, *JHEP* **02** (2022) 106 [arXiv:2111.04748] [INSPIRE].

[44] M. Krämer, T. Plehn, M. Spira and P.M. Zerwas, *Pair production of scalar leptoquarks at the Tevatron*, *Phys. Rev. Lett.* **79** (1997) 341 [hep-ph/9704322] [INSPIRE].

[45] M. Krämer, T. Plehn, M. Spira and P.M. Zerwas, *Pair production of scalar leptoquarks at the CERN LHC*, *Phys. Rev. D* **71** (2005) 057503 [hep-ph/0411038] [INSPIRE].

[46] J.B. Hammett and D.A. Ross, *NLO Leptoquark Production and Decay: The Narrow-Width Approximation and Beyond*, *JHEP* **07** (2015) 148 [arXiv:1501.06719] [INSPIRE].

[47] T. Mandal, S. Mitra and S. Seth, *Pair Production of Scalar Leptoquarks at the LHC to NLO Parton Shower Accuracy*, *Phys. Rev. D* **93** (2016) 035018 [arXiv:1506.07369] [INSPIRE].

[48] C. Borschensky, B. Fuks, A. Kulesza and D. Schwartländer, *Scalar leptoquark pair production at hadron colliders*, *Phys. Rev. D* **101** (2020) 115017 [arXiv:2002.08971] [INSPIRE].

[49] L. Buonocore, U. Haisch, P. Nason, F. Tramontano and G. Zanderighi, *Lepton-Quark Collisions at the Large Hadron Collider*, *Phys. Rev. Lett.* **125** (2020) 231804 [arXiv:2005.06475] [INSPIRE].

[50] L. Buonocore, P. Nason, F. Tramontano and G. Zanderighi, *Leptons in the proton*, *JHEP* **08** (2020) 019 [arXiv:2005.06477] [INSPIRE].

[51] A. Greljo and N. Selimovic, *Lepton-Quark Fusion at Hadron Colliders, precisely*, *JHEP* **03** (2021) 279 [arXiv:2012.02092] [INSPIRE].

[52] U. Haisch and G. Polesello, *Resonant third-generation leptoquark signatures at the Large Hadron Collider*, *JHEP* **05** (2021) 057 [arXiv:2012.11474] [INSPIRE].

[53] C. Borschensky, B. Fuks, A. Kulesza and D. Schwartländer, *Scalar leptoquark pair production at the LHC: precision predictions in the era of flavour anomalies*, *JHEP* **02** (2022) 157 [arXiv:2108.11404] [INSPIRE].

[54] A. Alves, O.J.P. Éboli, G. Grilli Di Cortona and R.R. Moreira, *Indirect and monojet constraints on scalar leptoquarks*, *Phys. Rev. D* **99** (2019) 095005 [arXiv:1812.08632] [INSPIRE].

[55] P. Nason, *A New method for combining NLO QCD with shower Monte Carlo algorithms*, *JHEP* **11** (2004) 040 [hep-ph/0409146] [INSPIRE].

[56] S. Frixione, P. Nason and C. Oleari, *Matching NLO QCD computations with Parton Shower simulations: the POWHEG method*, *JHEP* **11** (2007) 070 [`arXiv:0709.2092`] [ɪɴSPIRE].

[57] S. Alioli, P. Nason, C. Oleari and E. Re, *A general framework for implementing NLO calculations in shower Monte Carlo programs: the POWHEG BOX*, *JHEP* **06** (2010) 043 [`arXiv:1002.2581`] [ɪɴSPIRE].

[58] J.C. Pati and A. Salam, *Lepton Number as the Fourth Color*, *Phys. Rev. D* **10** (1974) 275 [*Erratum ibid.* **11** (1975) 703] [ɪɴSPIRE].

[59] J.C. Pati and A. Salam, *Unified Lepton-Hadron Symmetry and a Gauge Theory of the Basic Interactions*, *Phys. Rev. D* **8** (1973) 1240 [ɪɴSPIRE].

[60] W. Buchmüller, R. Ruckl and D. Wyler, *Leptoquarks in Lepton-Quark Collisions*, *Phys. Lett. B* **191** (1987) 442 [*Erratum ibid.* **448** (1999) 320] [ɪɴSPIRE].

[61] I. Doršner, S. Fajfer, A. Greljo, J.F. Kamenik and N. Košnik, *Physics of leptoquarks in precision experiments and at particle colliders*, *Phys. Rept.* **641** (2016) 1 [`arXiv:1603.04993`] [ɪɴSPIRE].

[62] A. Alloul, N.D. Christensen, C. Degrande, C. Duhr and B. Fuks, *FeynRules 2.0 — A complete toolbox for tree-level phenomenology*, *Comput. Phys. Commun.* **185** (2014) 2250 [`arXiv:1310.1921`] [ɪɴSPIRE].

[63] T. Hahn, *Generating Feynman diagrams and amplitudes with FeynArts 3*, *Comput. Phys. Commun.* **140** (2001) 418 [`hep-ph/0012260`] [ɪɴSPIRE].

[64] T. Hahn, S. Paßehr and C. Schappacher, *FormCalc 9 and Extensions*, *PoS* **LL2016** (2016) 068 [*J. Phys. Conf. Ser.* **762** (2016) 012065] [`arXiv:1604.04611`] [ɪɴSPIRE].

[65] T. Hahn and M. Pérez-Victoria, *Automatized one loop calculations in four-dimensions and D-dimensions*, *Comput. Phys. Commun.* **118** (1999) 153 [`hep-ph/9807565`] [ɪɴSPIRE].

[66] H.H. Patel, *Package-X: A Mathematica package for the analytic calculation of one-loop integrals*, *Comput. Phys. Commun.* **197** (2015) 276 [`arXiv:1503.01469`] [ɪɴSPIRE].

[67] S. Frixione, Z. Kunszt and A. Signer, *Three jet cross-sections to next-to-leading order*, *Nucl. Phys. B* **467** (1996) 399 [`hep-ph/9512328`] [ɪɴSPIRE].

[68] S. Frixione, *A General approach to jet cross-sections in QCD*, *Nucl. Phys. B* **507** (1997) 295 [`hep-ph/9706545`] [ɪɴSPIRE].

[69] A. Crivellin, C. Greub, D. Müller and F. Saturnino, *Scalar Leptoquarks in Leptonic Processes*, *JHEP* **02** (2021) 182 [`arXiv:2010.06593`] [ɪɴSPIRE].

[70] NNPDF collaboration, *The path to proton structure at 1% accuracy*, *Eur. Phys. J. C* **82** (2022) 428 [`arXiv:2109.02653`] [ɪɴSPIRE].

[71] T. Sjöstrand et al., *An introduction to PYTHIA 8.2*, *Comput. Phys. Commun.* **191** (2015) 159 [`arXiv:1410.3012`] [ɪɴSPIRE].

[72] P. Ciafaloni and D. Comelli, *Sudakov enhancement of electroweak corrections*, *Phys. Lett. B* **446** (1999) 278 [`hep-ph/9809321`] [ɪɴSPIRE].

[73] M. Cacciari, G.P. Salam and G. Soyez, *The anti-$k_t$ jet clustering algorithm*, *JHEP* **04** (2008) 063 [`arXiv:0802.1189`] [ɪɴSPIRE].

[74] M. Cacciari, G.P. Salam and G. Soyez, *FastJet User Manual*, *Eur. Phys. J. C* **72** (2012) 1896 [`arXiv:1111.6097`] [ɪɴSPIRE].

[75] ATLAS collaboration, *ATLAS b-jet identification performance and efficiency measurement with tt̄ events in pp collisions at $\sqrt{s} = 13$ TeV*, *Eur. Phys. J. C* **79** (2019) 970 [arXiv:1907.05120] [INSPIRE].

[76] ATLAS collaboration, *Muon reconstruction performance of the ATLAS detector in proton-proton collision data at $\sqrt{s} = 13$ TeV*, *Eur. Phys. J. C* **76** (2016) 292 [arXiv:1603.05598] [INSPIRE].

[77] ATLAS collaboration, *Performance of the ATLAS muon triggers in Run 2*, 2020 *JINST* **15** P09015 [arXiv:2004.13447] [INSPIRE].

[78] E. Conte, B. Fuks and G. Serret, *MadAnalysis 5, A User-Friendly Framework for Collider Phenomenology*, *Comput. Phys. Commun.* **184** (2013) 222 [arXiv:1206.1599] [INSPIRE].

[79] DELPHES 3 collaboration, *DELPHES 3, A modular framework for fast simulation of a generic collider experiment*, *JHEP* **02** (2014) 057 [arXiv:1307.6346] [INSPIRE].

[80] CMS collaboration, *Identification of hadronic tau lepton decays using a deep neural network*, 2022 *JINST* **17** P07023 [arXiv:2201.08458] [INSPIRE].

[81] CMS collaboration, *Identification of heavy-flavour jets with the CMS detector in pp collisions at* 13 *TeV*, 2018 *JINST* **13** P05011 [arXiv:1712.07158] [INSPIRE].

[82] E. Bols, J. Kieseler, M. Verzetti, M. Stoye and A. Stakia, *Jet Flavour Classification Using DeepJet*, 2020 *JINST* **15** P12012 [arXiv:2008.10519] [INSPIRE].

[83] ATLAS collaboration, *Search for neutral Higgs bosons of the minimal supersymmetric standard model in pp collisions at $\sqrt{s} = 8$ TeV with the ATLAS detector*, *JHEP* **11** (2014) 056 [arXiv:1409.6064] [INSPIRE].

[84] ATLAS collaboration, *Search for pairs of scalar leptoquarks decaying into quarks and electrons or muons in $\sqrt{s} = 13$ TeV pp collisions with the ATLAS detector*, *JHEP* **10** (2020) 112 [arXiv:2006.05872] [INSPIRE].

[85] ATLAS collaboration, *Search for new phenomena in pp collisions in final states with tau leptons, b-jets, and missing transverse momentum with the ATLAS detector*, *Phys. Rev. D* **104** (2021) 112005 [arXiv:2108.07665] [INSPIRE].

[86] G. Cowan, K. Cranmer, E. Gross and O. Vitells, *Asymptotic formulae for likelihood-based tests of new physics*, *Eur. Phys. J. C* **71** (2011) 1554 [*Erratum ibid.* **73** (2013) 2501] [arXiv:1007.1727] [INSPIRE].

[87] S. Alioli et al., *The POWHEG BOX*, (2022) http://powhegbox.mib.infn.it.

[88] J.C. Collins and D.E. Soper, *Angular Distribution of Dileptons in High-Energy Hadron Collisions*, *Phys. Rev. D* **16** (1977) 2219 [INSPIRE].

[89] D. Binosi, J. Collins, C. Kaufhold and L. Theussl, *JaxoDraw: A Graphical user interface for drawing Feynman diagrams. Version 2.0 release notes*, *Comput. Phys. Commun.* **180** (2009) 1709 [arXiv:0811.4113] [INSPIRE].

[90] H. Qu and L. Gouskos, *ParticleNet: Jet Tagging via Particle Clouds*, *Phys. Rev. D* **101** (2020) 056019 [arXiv:1902.08570] [INSPIRE].

[91] ATLAS collaboration, *Direct constraint on the Higgs-charm coupling from a search for Higgs boson decays into charm quarks with the ATLAS detector*, *Eur. Phys. J. C* **82** (2022) 717 [arXiv:2201.11428] [INSPIRE].

[92] CMS collaboration, *Search for Higgs boson decay to a charm quark-antiquark pair in proton-proton collisions at $\sqrt{s} = 13$ TeV*, arXiv:2205.05550 [INSPIRE].